Two displacive ferroelectric phase transitions in multiferroic quadruple perovskite BiMn$_7$O$_{12}$

A. Maia [1], M. Kempa [1], V. Bovtun [1], R. Vilarinho [2], C. Kadlec [1], J. Agostinho Moreira [2], A. A. Belik [3], P. Proschek [4], and S. Kamba [1,*]

[1]*Institute of Physics of the Czech Academy of Sciences, Na Slovance 2, 182 00 Prague 8, Czech Republic*

[2]*IFIMUP, Physics and Astronomy Department, Faculty of Sciences, University of Porto, Rua do Campo Alegre 687, s/n 4169-007 Porto, Portugal*

[3]*Research Center for Materials Nanoarchitectonics (MANA), National Institute for Materials Science (NIMS), Namiki 1-1, Tsukuba, Ibaraki 305-0044, Japan*

[4]*Faculty of Mathematics and Physics, Charles University, Ke Karlovu 5, 121 16 Prague, Czech Republic*

We report on the microwave, terahertz (THz), infrared, and Raman spectroscopic studies of BiMn$_7$O$_{12}$ ceramics, shedding more light onto the nature of two structural phase transitions and their possible relation with ferroelectricity in this compound. We observed a softening of one polar phonon in the THz range on cooling towards 460 and 300 K, i.e., temperatures at which BiMn$_7$O$_{12}$ undergoes subsequent structural phase transitions from monoclinic $I2/m$ to polar monoclinic Im and triclinic $P1$ phases. The soft phonon causes dielectric anomalies typical for displacive ferroelectric phase transitions. Microwave measurements performed at 5.8 GHz up to 400 K qualitatively confirmed not only the dielectric anomaly at 300 K, but also revealed two other weak dielectric anomalies near the magnetic phase transitions at 60 and 28 K. This evidences the multiferroic nature of the low-temperature phases, although the relatively high conductivity in the kHz and Hz spectral range prevented us from directly measuring the permittivity and ferroelectric polarization. Some Raman modes sense the magnetic phase transitions occurring near 60 and 25 K, showing that spin-phonon coupling is relevant in this compound and in this temperature range. The deviation of the Mn-O stretching mode frequency from the anharmonic temperature behavior was successfully explained by the spin correlation function calculated from the magnetic contribution to the specific heat.

I. INTRODUCTION

A-site ordered quadruple perovskites, $AA'_3B_4O_{12}$, exhibit several interesting physical and chemical properties [1,2], such as reentrant structural transitions [3], intersite charge transfer and disproportionation [2], giant dielectric constant [4,5], multiferroicity [6,7], and high catalytic activity [8]. $AA'_3B_4O_{12}$ has a 12-fold-coordinated *A* site and a square-planar-coordinated *A'* site, while *B* sites have the usual octahedral coordination for perovskites. For manganese, it is possible to have $A' = B$, and the composition can be written as AMn$_7$O$_{12}$ in brief. These manganites can have spin, orbital, and charge degrees of freedom depending on the oxidation state of the *A* cation [1,3,6,9–12].

The quadruple perovskite BiMn$_7$O$_{12}$ exhibits three structural and two magnetic phase transitions [13]. Above $T_1 = 608$ K, BiMn$_7$O$_{12}$ crystallizes in a parent cubic structure, with space group $Im\bar{3}$. Between 460 and 608 K, BiMn$_7$O$_{12}$ adopts a monoclinic symmetry, with pseudo-orthorhombic metrics [denoted as $I2/m(o)$], and orbital order appears below T_1. At $T_2 = 460$ K, BiMn$_7$O$_{12}$ undergoes a phase transition into a polar monoclinic structure, described by the Im space group. Finally, at $T_3 = 290$ K, a triclinic distortion takes

place and BiMn$_7$O$_{12}$ transits into another polar structure, described by the $P1$ space group (assigned as $I1$ in Ref. [14]). Structural analyses of BiMn$_7$O$_{12}$ are challenging because of severe domain twinning in single crystals, and anisotropic broadening and diffuse scattering in powder [13]. However, first-principles calculations confirm that noncentrosymmetric structures are more stable than centrosymmetric ones [13]. The energy difference between the Im and $P1$ models is very small, and this fact can explain why the Im to $P1$ transition is very gradual, and there are no differential scanning calorimetry (DSC) anomalies associated with this transition [13]. The crystal structure and phase sequence of BiMn$_7$O$_{12}$ are illustrated in Fig. 1.

In earlier studies, BiMn$_7$O$_{12}$ has been shown to exhibit two magnetic phase transitions at 55 and 25 K [16,17]. Recent magnetic and powder neutron diffraction experiments revealed three successive magnetic phase transitions [18]. Below $T_{N1} = 59$ K, *B*-site Mn cations order antiferromagnetically with propagation vector $k_1 = (0.5, 0, -0.5)$, and at $T_{N2} = 55$ K the *A'*-site Mn spins order ferrimagnetically with $k_2 = (0, 0, 0)$ [18]. Both magnetic orderings coincide down to $T_{N3} = 27$ K, below which both the *A'*-site and *B*-site spins reorient with modulation vector $k_3 = (0, 1, 0)$. It should be noted that, in contrast to other type II multiferroics, the polar distortion of the lattice in the $P1$ structure of BiMn$_7$O$_{12}$ stabilizes the E-type magnetic ordering of Mn at the *B*-site
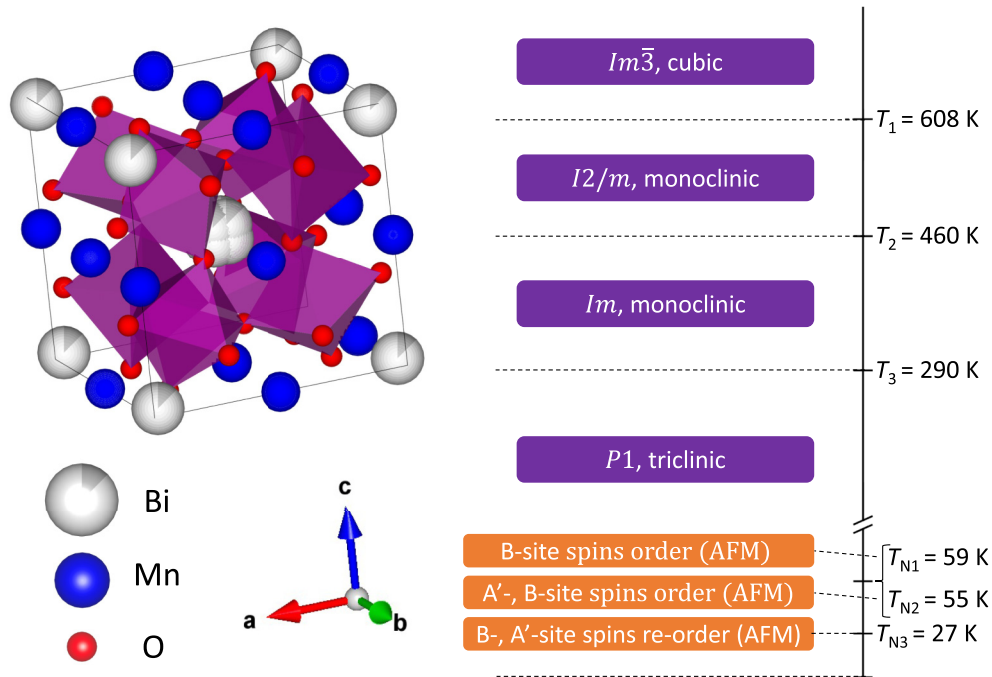
*kamba@fzu.cz

FIG. 1. Crystal structure of $BiMn_7O_{12}$ at room temperature and schematic representation of its structural (purple) and magnetic (orange) phase sequence. The illustration of the crystal structure was obtained using VESTA software [15].

perovskite positions due to trilinear coupling of two magnetic order parameters η_1, η_2 and polarization P, i.e., $\eta_1\eta_2P$ [18]. Conversely, in $BiMn_3Cr_4O_{12}$, a different mechanism should be responsible for stabilizing the magnetic structure (probably with a quadratic coupling η^2P or ηP^2), because in this material only the Cr spins order below $T_N = T_{FE}$ [7]. Magnetoelectric coupling should be induced in both materials via inverse exchange striction ($\propto S_i \cdot S_j$). The magnetic phase sequence and the crystal structure are depicted in Fig. 1 [16–18].

The relation between the local crystal structure and the spontaneous electric polarization in $BiMn_{6.96}Fe_{0.04}O_{12}$ was recently studied using ^{57}Fe probe Mössbauer spectroscopy [19,20]. A "dynamic" Born charge model was used to develop an algorithm to construct the temperature dependence of the polarization of the crystal using structural data of the compound and the experimental values of the quadrupole splittings of the Mössbauer spectra of the ^{57}Fe probe atoms [19]. The temperature dependence of the electric polarization obtained from the Mössbauer data points out for a paraelectric to ferroelectric first-order phase transition with $T_c \approx 437$ K, close to the $I2/m$ to Im structural transition temperature T_2, as well as a considerable increase in the electric polarization below 270 K, with extrapolated $T^* \approx 294$ K, close to the Im to $P1$ structural transition at T_3 [19]. It has also been demonstrated that light hole doping of $BiMn_7O_{12}$ with Cu ($BiCu_{0.1}Mn_{6.9}O_{12}$) can induce incommensurate helical ordering of electric dipoles [21].

Despite $BiMn_7O_{12}$ structural and magnetic properties being extensively studied in the recent past, its dielectric and possible ferroelectric properties have not yet been published due to its relatively high conductivity above 100 K. $BiMn_7O_{12}$ is sufficiently resistive to perform permittivity measurements only below 90 K, revealing dielectric anomalies at magnetic phase transitions [22,23]. This evidences for

magnetodielectric coupling and the possible multiferroic nature of the low temperature magnetic phases. However, direct electric polarization measurements have not yet been published due to the impossibility of applying a sufficiently high electric field in the measurement of ferroelectric hysteresis loops, and of poling the sample in the paraelectric phase for pyroelectric current studies, due to its high conductivity.

Spectroscopic methods that are insensitive to the conductivity of the sample are used to uncover the nature of structural and possible ferroelectric phase transitions in $BiMn_7O_{12}$. That is why we have undertaken a comprehensive temperature dependent heat capacity, infrared, THz, Raman, and microwave measurements in a broad temperature range, revealing a ferroelectric soft mode driving both ferroelectric phase transitions near 460 and 290 K, and optical phonons showing anomalies near magnetic phase transitions. In addition, we also observed dielectric anomalies at two magnetic phase transitions, indicative of magnetoelectric coupling in multiferroic phases.

II. EXPERIMENTAL DETAILS

$BiMn_7O_{12}$ polycrystalline samples were synthesized under high-pressure and high-temperature conditions from stoichiometric mixtures of Bi_2O_3 and Mn_2O_3 starting reagents, as detailed in Ref. [13]. Laboratory powder x-ray diffraction (XRD) data were taken at room temperature using a MiniFlex600 diffractometer with CuK_α radiation (2θ range 10–80°, a step width of 0.02°, and a counting speed of 1°/min). XRD data were analyzed by the Rietveld method with RIETAN-2000 program [24]. Weight fractions of impurities were estimated by RIETAN-2000 from refined scale factors. The best ceramics contained some impurities, specifically 1% of $Bi_2O_2CO_3$ and 1% Mn_2O_3. The ceramic disks with diameter 6 mm had thickness 1–2 mm. Scanning electron

microscope images of BiMn$_7$O$_{12}$ ceramics revealed grains with the size 2–5 μm (see Fig. S1 in the Supplemental Material [25]). The microwave response at 5.8 GHz was measured using the composite dielectric resonator method [27,28]. The TE$_{01\delta}$ resonance frequency, quality factor, and insertion loss of the base cylindrical dielectric resonator with and without the sample were recorded during heating from 10 to 400 K with a temperature rate of 0.5 K/min in a Janis closed-cycle He cryostat. The sample without electrodes (2 × 2 mm plate, 0.32 mm thick) was placed on top of the base dielectric resonator. The resonators were measured in the cylindrical shielding cavity using the transmission setup with a weak coupling by an Agilent E8364B network analyzer. The complex refractive index $n = \sqrt{\epsilon\mu}$ of the sample(s) was calculated from the acquired resonance frequencies and quality factors of the base and composite resonators.

The magnetic properties were measured via vibrating sample magnetometer (VSM, Quantum Design) using a Quantum Design physical properties measurement system (PPMS) in various temperature ranges (down to 2 K) and magnetic field (up to 9 T). The heat capacity measurements were performed by using the heat capacity option in the PPMS in various ranges of temperature (down to 2 K).

The THz complex transmittance was measured using a custom-made time-domain spectrometer powered by a Ti:sapphire femtosecond laser with 35-fs-long pulses centered at 800 nm. The system is based on coherent generation and subsequent coherent detection of ultrashort THz transients. The detection scheme consists of an electro-optic sampling of the electric field of the transients within a 1-mm-thick, (110)-oriented ZnTe crystal as a sensor [29]. This allows measuring the time profile of the THz transients transmitted through the sample. The BiMn$_7$O$_{12}$ sample was highly absorbing in the THz region due to a strong optical soft mode, therefore we glued it on a sapphire substrate and polished it down to 38 μm. The bare sapphire substrate (thickness 0.543 mm) was measured as a reference.

Low-temperature unpolarized IR reflectivity measurements of one-sided optically polished ceramics (thickness ∼1.5 mm) were performed using a Bruker IFS-113v Fourier-transform IR spectrometer equipped with a liquid-He-cooled Si bolometer (1.6 K) serving as a detector. For both the THz complex transmittance and IR reflectivity measurements, the temperature control was done through an Oxford Instruments Optistat optical continuous He-flow cryostats with mylar and polyethylene windows, respectively. A commercial high-temperature cell Specac P/N 5850 was used for IR and THz studies above room temperature. The samples were heated in vacuum up to 580 K. We were concerned about heating the samples to higher temperatures to prevent degradation of the samples. The IR spectra were fitted using one Lorentz oscillator for each phonon mode. The complex dielectric function is given by

$$\varepsilon(\omega) = \varepsilon_\infty + \sum_j \frac{\Delta\varepsilon_j \omega_{0j}^2}{\omega_{0j}^2 - \omega^2 - i\gamma_j\omega}, \quad (1)$$

where ε_∞ is the contribution from electronic transitions to the dielectric function, and the jth phonon is described by an eigenfrequency ω_{0j}, an oscillator strength $\Delta\varepsilon_j$, and

damping γ_j. These parameters were fitted so that the reflectivity at normal incidence, given by $R(\omega) = |\frac{\sqrt{\varepsilon(\omega)}-1}{\sqrt{\varepsilon(\omega)}+1}|^2$, matches the experimental data. The eigenfrequencies ω_{0j} correspond to the transverse optical phonon frequencies. The high-frequency permittivity ε_∞ was obtained from the room-temperature frequency-independent reflectivity tail above the phonon frequencies and was assumed temperature independent.

Unpolarized Raman spectra were recorded using a Renishaw inVia Qontor spectrometer with a 785-nm linearly polarized diode-pumped laser and an edge filter. Measurements were done at fixed temperatures from 10 to 600 K using a THMS600 Linkam stage cooled by a nitrogen flow down to 80 K and a custom-made closed-cycle helium cryostat down to 10 K. The laser power (2.3 mW) was chosen adequately to prevent heating the sample. The wave number at a given temperature $\omega(T)$ of each Raman mode is obtained by the best fit of the Raman spectra with a sum of damped oscillators [30]:

$$I(\omega, T) = [1 + n(\omega, T)] \sum_j \frac{A_{0j}\Omega_{0j}^2\Gamma_{0j}\omega}{\left(\Omega_{0j}^2 - \omega^2\right)^2 + \Gamma_{0j}^2\omega^2}, \quad (2)$$

where $n(\omega, T)$ is the Bose-Einstein factor and A_{0j}, Ω_{0j}, Γ_{0j} are the strength, wave number, and damping coefficient of the jth oscillator, respectively. In the temperature range where no anomalous behavior is observed, the temperature dependence of the wave number of the phonon frequencies is well described by the normal anharmonic temperature effect due to volume contraction as temperature decreases [31]:

$$\omega(T) = \omega_0 + C\left[1 + \frac{2}{e^x - 1}\right] + D\left[1 + \frac{3}{e^y - 1} + \frac{3}{(e^y - 1)^2}\right] \quad (3)$$

with $x \equiv \hbar\omega_0/2k_BT$, $y \equiv \hbar\omega_0/3k_BT$, and where ω_0, C, and D are model constants, $\hbar$ is the reduced Planck constant, and k_B is the Boltzmann constant.

Deviations to the normal anharmonic temperature effect were interpreted on the basis of the spin-phonon coupling as [32]

$$\Delta\omega(T) = \omega(T) - \omega_0 \propto \frac{\partial^2 J}{\partial u^2}\langle S_i \cdot S_j\rangle \approx R\langle S_i \cdot S_j\rangle \quad (4)$$

where J is the magnetic exchange integral, u is the normal coordinate of the vibrational mode, and R is the difference of the second derivatives of the ferro- and antiferromagnetic exchange integrals with respect to the normal coordinate, where the approximation assumes the same spin correlation function, $\langle S_i \cdot S_j\rangle$, for both.

III. RESULTS AND DISCUSSION

A. Polar soft phonon in the THz range

Figures 2(a) and 2(b) show the real and imaginary parts of the complex dielectric spectra, $\varepsilon'(\omega)$ and $\varepsilon''(\omega)$ of BiMn$_7$O$_{12}$, respectively, measured at several fixed temperatures in the THz spectral range. At 580 K, only one polar phonon is observed at 28 cm^{-1}. As the temperature decreases towards $T_2 = 460$ K, the phonon frequency shifts towards lower frequencies, while the static permittivity increases, and on further
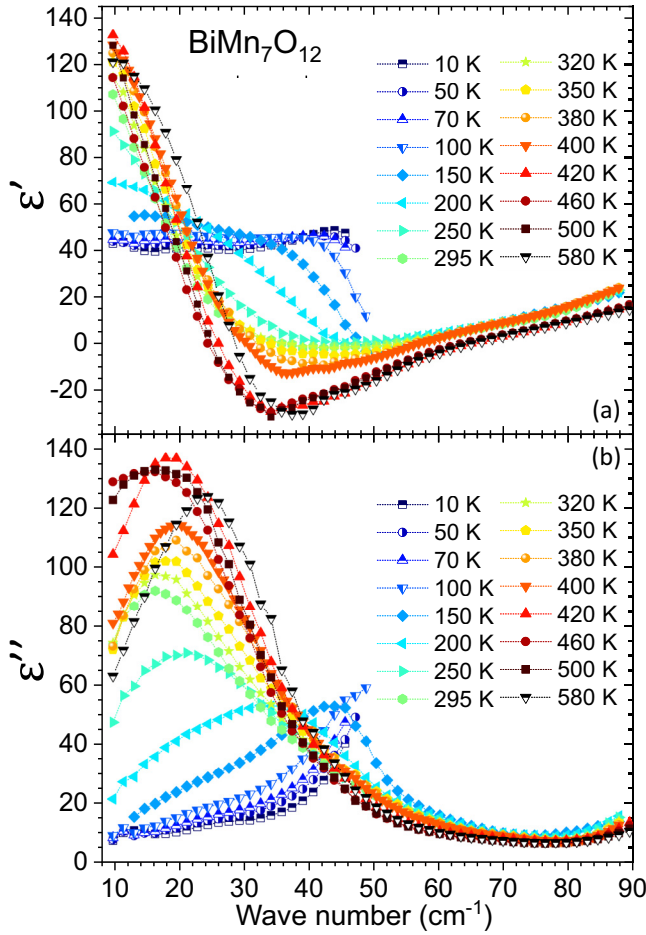
FIG. 2. (a) $\varepsilon'(\omega)$ and (b) $\varepsilon''(\omega)$ spectra of $BiMn_7O_{12}$ obtained by THz time-domain spectroscopy at several temperatures.

FIG. 3. (a) Temperature dependence of the frequency of two components of the soft mode in $BiMn_7O_{12}$, $\omega_{02} = \omega_{SM}$ and ω_{01}, where the latter is discernable only below room temperature. (b) Temperature dependence of dielectric strength of the soft mode and the sum of the contributions of all phonons to the static permittivity. The dashed lines are a guide for the eye. Inset: Contribution (in %) of the SM to the total static permittivity.

cooling to 380 K, the phonon hardens. This temperature behavior is typical of a polar soft phonon driving a displacive ferroelectric phase transition. Below 380 K, the phonon softens once again down to 300 K. This phonon anomaly at 300 K is in the vicinity of the structural phase transition from the Im to $P1$ structure, in which the ferroelectric polarization is predicted to move out of the ac plane [18]. Below 300 K, the phonon frequency smoothly increases down to 10 K. This behavior is best seen in the temperature dependence of the soft mode wave number and its dielectric strength, depicted in Figs. 3(a) and 3(b), respectively. The dielectric strength of the soft phonon, $\Delta\varepsilon_{SM}(T)$, considerably increases on cooling from 580 K towards 460 K [see Fig. 3(b)] due to the conservation law of the oscillator strength $f_j = \Delta\varepsilon_j(T)\omega_{0j}^2(T) =$ const (valid for all uncoupled polar phonons, including the soft mode). It is noteworthy that at 580 K, $\Delta\varepsilon_{SM}$ constitutes approximately 90% of the static electric permittivity in the THz range: $\varepsilon_0 = \varepsilon_\infty + \sum_j \Delta\varepsilon_j$. Cooling from 380 K, $\Delta\varepsilon_{SM}(T)$ decreases and exhibits a broad plateaulike behavior down to 300 K, below which it smoothly decreases down to 20% of the static electric permittivity at the lowest measured temperature.

The temperature dependence of the relative changes of real and imaginary parts of the dielectric permittivity measured at
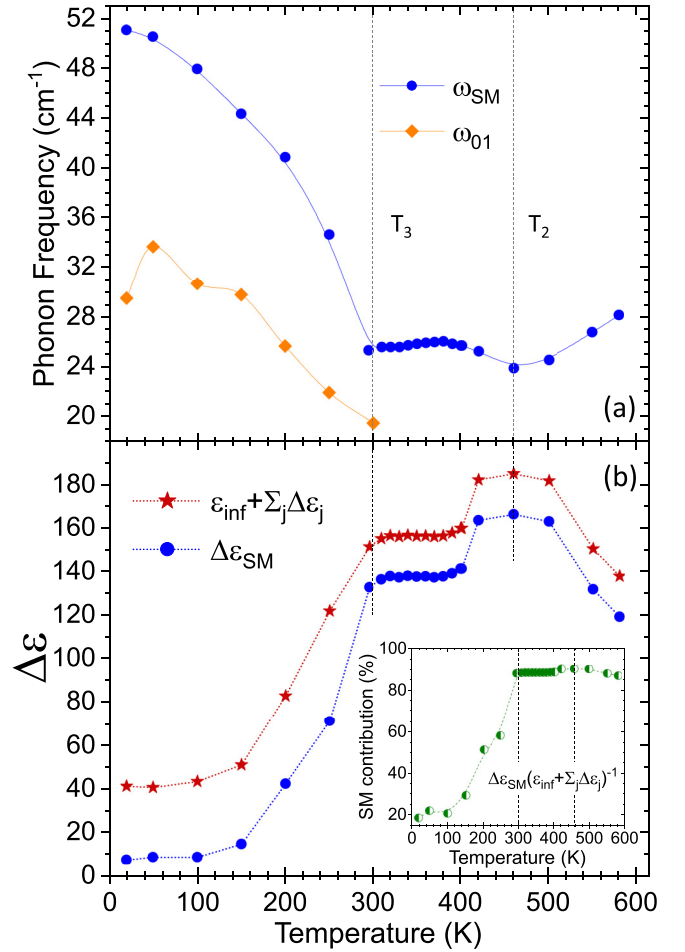
5.8 GHz, is shown in Figs. 4(a) and 4(b), respectively. A broad anomaly at 300 K is clearly visible, which is qualitatively consistent with the phonon anomaly in Fig. 3 near T_3. Its absolute value is smaller than ε in Fig. 3, most likely due to lower accuracy of the microwave (MW) measurements, because the rectangular sample plate is much smaller than base dielectric resonator while the exact calculation of ε requires the same diameter of the cylindrical sample and base resonator [27]. The anomalies seen at magnetic phase transitions near 60 and 28 K (see also our magnetic moment measurements in Fig. S2 [25]) can come from both magnetic permeability μ and electric permittivity ε, but it should be mentioned that dielectric measurements at 100 kHz revealed similar anomalies in $\varepsilon(T)$ [23] and also in the Hz frequency range (see Fig. S3 of the Supplemental Material [25]), so we assume that the anomalies observed at low temperatures in Fig. 4 also come from $\varepsilon(T)$ and not from $\mu(T)$. The existence of dielectric anomalies at the magnetic phase transition temperatures is also in agreement with Ref. [18] which, based on a detailed analysis of
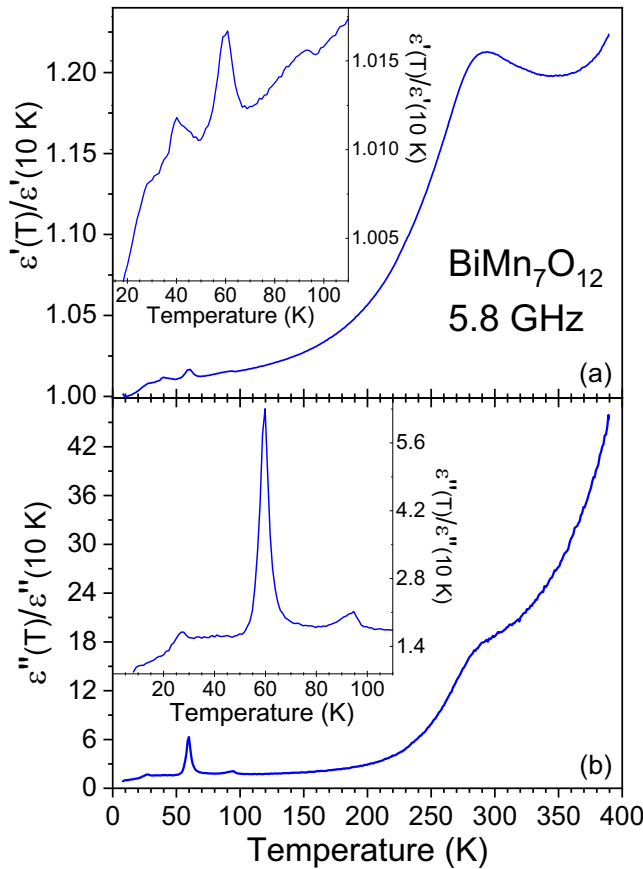
FIG. 4. Relative changes of the (a) real and (b) imaginary parts of the dielectric permittivity measured at 5.8 GHz.

neutron powder diffraction data, revealed that the magneto-electric coupling via inverse exchange striction, expressed by trilinear coupling of the order parameters, uniquely stabilizes a polar collinear magnetic structure.

It should be mentioned that the dielectric anomalies seen at the magnetic phase transitions in the temperature dependence of permittivity, both in the microwave (Fig. 4) and low-frequency spectral range (Fig. S3 [25]), are not detected in the THz spectra, as the measurements were performed each 10 K, not exactly coinciding with the temperatures of the magnetic phase transitions. Moreover, the permittivity anomalies have values of 1–2 (see Fig. S3 [25]), which are comparable to the accuracy of the THz measurements.

Unfortunately, due to the experimental limitations of our MW setup, it was not possible to measure above 400 K, so the effect of the higher temperature structural transitions (T_1 and T_2) in the MW permittivity are not ascertained [15]. The origin of the small anomaly around 95 K is unknown, but it should be noted that, at the same temperature, a small anomaly in the temperature dependence of the magnetization was observed (see Fig. S2b [25]), but no anomaly in specific heat was seen near 95 K (see Fig. 7).

B. Polar phonons

To better describe the temperature dependence of the polar soft phonon and its contribution to the total permittivity, we
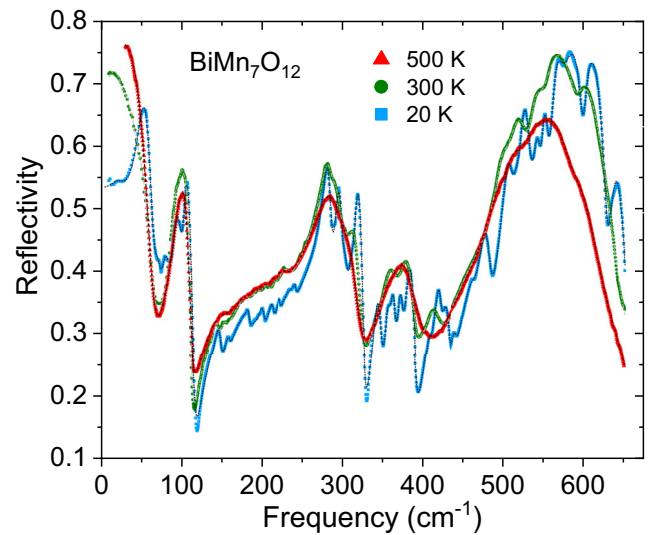

FIG. 5. Unpolarized IR reflectivity spectra of $BiMn_7O_{12}$ ceramics recorded at 20, 300, and 500 K. The corresponding fits are shown as dotted lines. The reflection band below $50\,cm^{-1}$ corresponds to the soft mode.
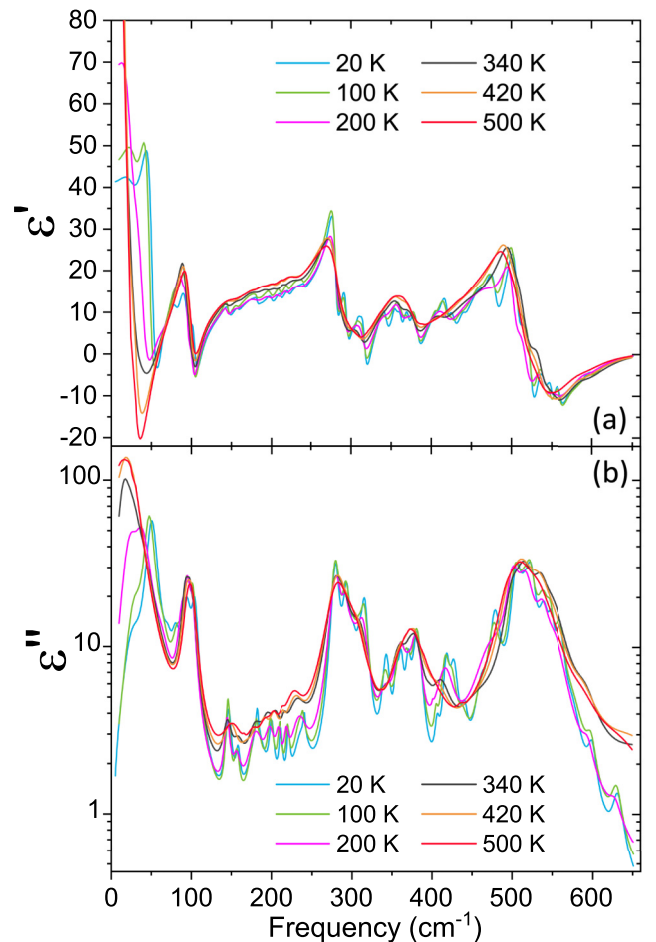

FIG. 6. (a) ε' and (b) ε'' (in logarithmic scale) spectra of $BiMn_7O_{12}$ obtained from fitting the IR reflectivity at several temperatures.

TABLE I. Factor-group analysis of the Γ-point phonons in $BiMn_7O_{12}$ [33–35]. The Wyckoff positions were taken from Ref. [13].

Temperature	Space group	IR-active modes	Raman-active modes	Silent modes	Acoustic modes
$T > T_1$	$Im\bar{3}$	$13T_u$	$3A_g \oplus 3E_g \oplus 7T_g$	$3A_u \oplus 3E_u$	$1T_u$
$T_2 < T < T_1$	$I2/m$	$19A_u \oplus 23B_u$	$13A_g \oplus 11B_g$		$1A_u \oplus 2B_u$
$T_3 < T < T_2$	Im	$32A' \oplus 25A''$	$32A' \oplus 25A''$		$2A' \oplus 1A''$
$T < T_3$	$P1$	$57A$	$57A$		$3A$

have also probed the higher energy polar lattice excitations through temperature dependent unpolarized Fourier transform infrared spectroscopy. Representative unpolarized reflectivity spectra, recorded at 20, 300, and 500 K, are shown in Fig. 5. The MIR spectrum at 300 K is shown in Fig. S4, and the fit parameters are listed in Table SI of the Supplemental Material [25]. The spectra of the real and imaginary parts of permittivity, calculated from fitting the IR reflectivity spectra using Eq. (1), are also shown in Figs. 6(a) and 6(b), respectively.

The factor-group analysis and the optical activity of phonons for the different structural phases is presented in Table I. The primitive cell contains only one formula unit $BiMn_7O_{12}$ in all crystal phases. From a symmetry point of view, 15 new polar modes and 33 new Raman modes become active due to a change of symmetry from monoclinic $I2/m$ to the lower symmetry monoclinic Im at 460 K. When changing from Im symmetry to $P1$ at 300 K, no new IR or Raman modes are expected. However, it should be emphasized that in the ferroelectric Im and $P1$ phases all phonons are both IR and Raman active.

It should be noted that the $I2/m$ structure contains 69 modes (including acoustic modes), although there are only 60 modes in the Im and $P1$ phases, at lower temperatures. This apparent discrepancy is due to the Bi cation being at Wyckoff position $8j$ with 1/4 occupancy in the $I2/m$ phase [13], so nine more modes are allowed than at lower temperatures. According to Ref. [13], in the cubic phase the Bi cation is in the Wyckoff position $16f$ with an occupation of only 1/8 and is therefore also predicted to have a higher number of degrees of freedom, and modes, than at lower temperatures. The partial occupation of atomic positions influences the increased damping of the corresponding phonons in the high-temperature phases.

The significant increase in the number of polar modes with cooling can be seen both in Figs. 5 and 6. Experimentally, we detected 41 IR-active modes at 20 K ($P1$ phase), 31 modes at 300 K (Im phase), and 28 modes at 500 K ($I2/m$ phase). This is below the number of modes expected from the factor-group analysis. Both the high number of modes and the temperature ranges of the phase transitions leading to a higher damping of the modes explain the lower number of detected modes. Furthermore, many of those modes can have an intensity that is below our detection limit.

The soft mode should have T_u symmetry in the cubic phase and should split in the monoclinic $I2/m$ phase below 608 K into three components with $A_u + 2B_u$ symmetries. Since $BiMn_7O_{12}$ chemically decomposes at high temperatures, it was possible to perform THz measurements only up to 580 K, when the soft mode must already be split into three components. The phonons with frequencies ω_{01}–ω_{03} are very likely the three components of the soft mode, although the mode ω_{03} is not seen at 500 K (see Table SI [25]) due to its low strength

and strong damping and only resolves below 380 K in Im phase. The two components of the soft mode with frequencies ω_{01} and ω_{02} lie below 30 cm^{-1}, but are overlapped above T_3, so that they can only be resolved in the $P1$ phase below 300 K, when they harden and their damping decreases with cooling (see Fig. 3).

C. Specific heat

The specific heat, divided by temperature, as a function of temperature, is shown in Fig. 7. Two anomalies are clearly observed in the temperature dependence of the specific heat at 59 and at 24 K, respectively. The temperatures at which these anomalies occur are in good agreement with the reported values of the critical temperatures of the magnetic phase transitions occurring at $T_{N1} = 59$ K and at $T_{N3} = 23$ K, respectively, associated with the paramagnetic to the E-type antiferromagnetic ordering of the B-site Mn^{3+} spins, and a change of spin ordering of both A'- and B-site Mn sublattices. As in previous reports, the specific heat does not reveal any anomalous temperature dependence at T_{N2} nor at the structural phase transitions occurring below 300 K. The analysis of the specific heat versus temperature, by means of the fitting of Debye's equation to the experimental data, enabled us to calculate the magnetic contribution to the specific heat, shown in Fig. 7 (neglecting the electronic contribution only relevant
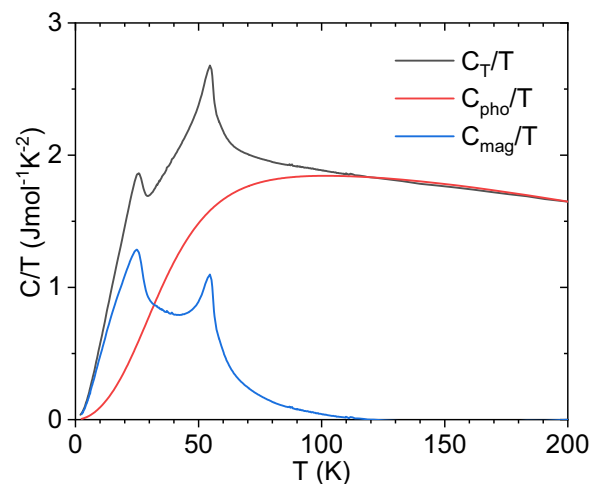

FIG. 7. Temperature dependence of the specific heat divided by temperature of $BiMn_7O_{12}$. Solid red line was determined by the best fit of Debye equation to the experimental data recorded above 120 K. Temperature dependence of the magnetic contribution to the specific heat, calculated from the difference of the experimental data and the extrapolated lattice contribution described by Debye behavior, extrapolated to 2 K.
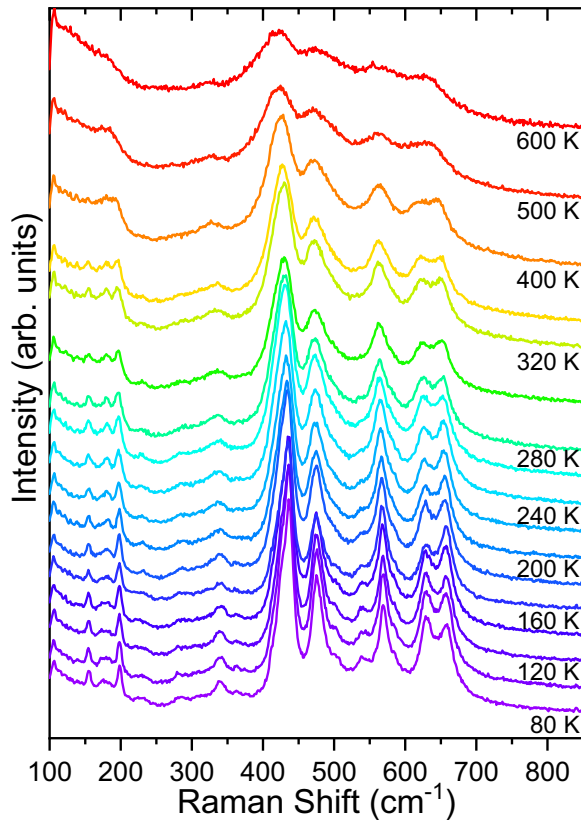
FIG. 8. Unpolarized Raman spectra of $BiMn_7O_{12}$ ceramics recorded at several fixed temperatures. The spectra are vertically offset from each other for better resolution.

below 10 K) [25]. The magnetic contribution to the specific heat increases just below 150 K, due to precursor magnetic effects. The existence of precursor effects well above the magnetic phase transition has been observed also in rare-earth orthomanganites, like $GdMnO_3$ [36].

D. Raman scattering and spin-phonon coupling

Figure 8 shows the unpolarized Raman spectra recorded at different fixed temperatures, in the 100–850 cm^{-1} spectral range. The energies of the Raman modes determined in three crystal phases are listed in Table SII [25]. The high temperature Raman spectra reveal rather broad bands, due to thermal effects. The Raman spectrum recorded at 600 K is properly simulated with seven bands in this spectral range. According to group theory arguments and published crystallographic data [13], in the $Im\bar{3}$ cubic symmetry only phonons involving vibrations of oxygen atoms are Raman active. As expected, on cooling, the Raman bands become narrower and shift towards higher wave numbers, according to Eq. (3). The phase transition at $T_1 = 608$ K impacts certain spectral features, with the most evident being the splitting of the band located at 175 and 633 cm^{-1}, at 600 K, and the appearance of sharp bands at 158 cm^{-1} in the spectrum recorded at 380 K. The spectrum recorded at 400 K is described by 12 bands. The structural phase transition from Im to $P1$, at 290 K is revealed by the appearance of weak bands, better observed in the 470–550 cm^{-1} range. However, the number of new

bands is smaller than the number of predicted new modes in the Raman spectra recorded in the monoclinic and triclinic phases; this discrepancy is explained by a weak intensity of modes and partial/total band overlap. Nevertheless, a detailed analysis of the temperature dependencies of the frequency of some phonons reveals interesting results, which we will address in the following.

Figure 9(a) shows the temperature dependence of the phonon frequency, observed at 153 cm^{-1} at 440 K. This phonon is only observed below $T_2 = 460$ K, and its frequency exhibits a cusplike anomaly at ~294 K, exactly at the Im to $P1$ structural phase transition. In rare-earth orthomanganites and rare-earth orthoferrites, low frequency phonons lying in this spectral range are assigned to the A-site atomic vibrations. The appearance of this band at the cubic ($Im\bar{3}$) to the monoclinic ($I2/m$) phase transition at T_2 reveals the Raman activation of vibrations involving other than just oxygen movements. Although no mode assignment is available to the best of our knowledge, we tentatively assign the phonon seen near 150 cm^{-1} to the A- or A'-site cation vibration, likely associated with Mn oscillations. This mode assignment is also supported by the current interpretation of the Raman spectra recorded in $LaMn_7O_{12}$ [37]. The ferroelectric polarization is caused mainly by displacement of Bi cations, but in the A perovskite positions there is not only Bi, but also three Mn cations which should sense the displacement of Bi cations, and therefore, the vibration of these Mn cations could also show a change in frequency at the ferroelectric phase transition from the Im to the $P1$ phase. The same phonon displays, above room temperature, an increasing damping when heating to $T_2 = 460$ K (Fig. S6 [25]). Since this phonon is highly damped above T_2, it is not possible to accurately determine its frequency in the $I2/m$ phase. A mode with a similar frequency is seen in the IR spectra, but its value shows a strong increase with heating (Fig. S6 [25]). Also, its attenuation is high at high temperatures, so its frequency is burdened with a large error, making it impossible to determine whether it is the same mode as in the Raman spectra (which is allowed by the selection rules in Table I) or a different mode entirely.

The magnetic phase transition occurring at $T_{N1} = 59$ K is also reflected by the anomalous temperature dependence of some internal vibrations. As a representative example, we present in Figs. 9(a) and 9(b) the temperature dependence of the modes at 559 cm^{-1} (value at 400 K) and 633 cm^{-1} (value at 600 K), respectively. These two modes are known to involve the oxygen vibrations and, consequently, they account for the changes in bond angle O-Mn-O and length Mn-O, respectively. Therefore, these vibrations probe the magnetic exchange interactions. On cooling, the wave number of these two modes increases, following the anharmonic temperature behavior described by the solid lines, determined by the fit of Eq. (3) to the experimental data above 200 K and extrapolated to low temperatures. No clear anomalies are ascertained in the structural phase transitions, but a detailed inspection of the temperature dependence of the wave number of these two modes shows a clear deviation from the extrapolated anharmonic temperature behavior. The deviation is clear at $T_{N1} = 59$ K; for further cooling, an anomalous increase is observed, due to spin-phonon coupling in this compound. As representative example, we focus on the Mn-O vibration at
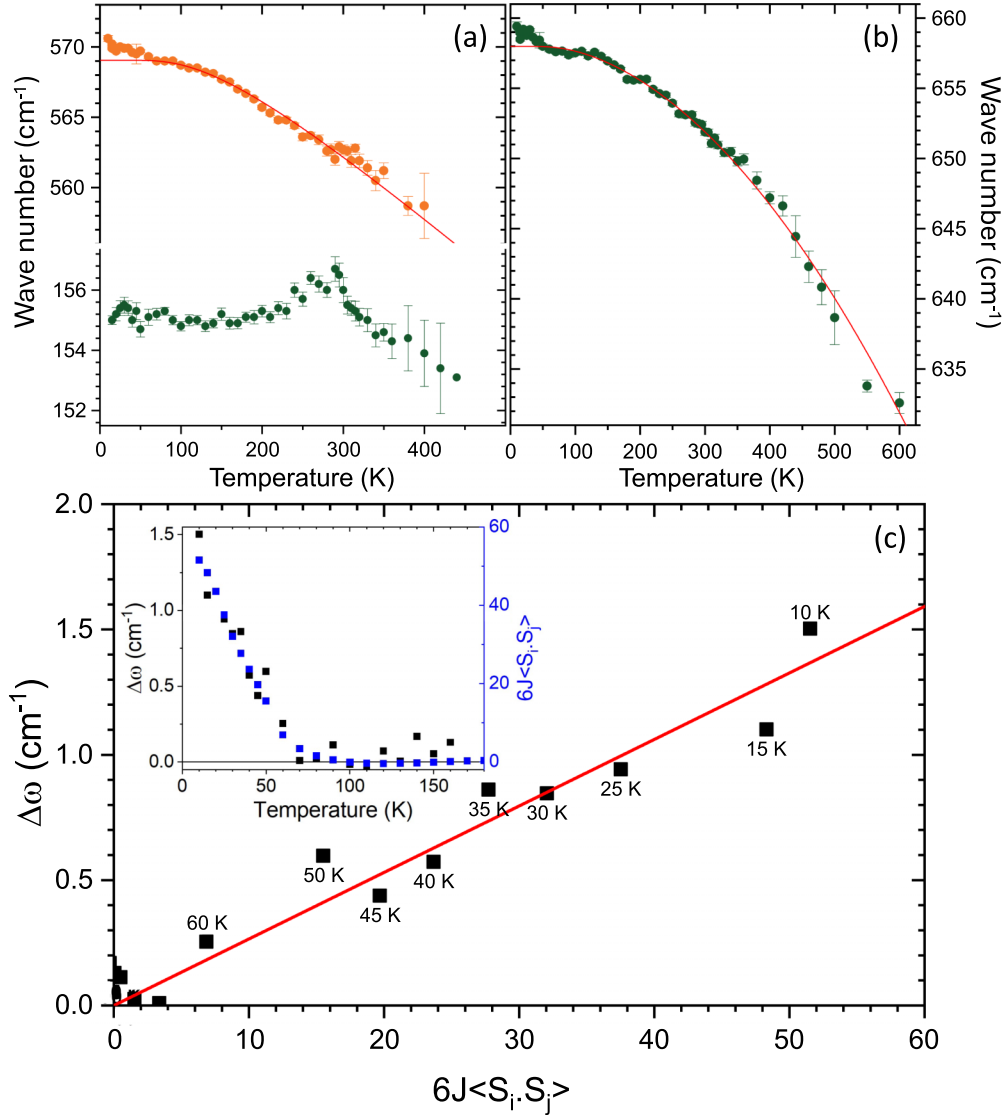
FIG. 9. (a),(b) Temperature dependence of the wave number of selected Raman modes. The best fit with Eq. (3) in the paraelectric phase is represented by a solid line and is extrapolated down to 0 K. (c) The deviation, $\Delta\omega$, of the highest phonon frequency seen near 650 cm^{-1} from the anharmonic temperature behavior [Eq. (3)] as a function of the spin-spin correlation function, $6J\langle \mathbf{S}_i \cdot \mathbf{S}_j \rangle$, obtained from integrating the magnetic contribution to the specific heat, shown in Fig. 7. Inset: temperature dependencies of $\Delta\omega$ and $6J\langle \mathbf{S}_i \cdot \mathbf{S}_j \rangle$.

$\sim$559 cm^{-1} (value at 400 K), shown in Fig. 9(a), which better senses the magnetic phase transition at T_{N1}. According to spin-phonon coupling theory presented in Eq. (4), the anomalous temperature dependence of the wave number must be a linear function of the spin-spin correlation function, $\langle \mathbf{S}_i \cdot \mathbf{S}_j \rangle$, which can be calculated from the integral of the magnetic contribution to the specific heat shown in Fig. 9 [32]. In this case, the anomalous temperature dependence of the wave number of the aforementioned Mn-O vibration is a linear function of the spin-spin correlation function, as shown in Fig. 9(c), providing clear evidence for the coupling between lattice vibrations and the magnetic momenta in BiMn$_7$O$_{12}$. Note that the spin-spin correlation function calculated from the magnetic contribution to the specific heat increases linearly below T_{N1} and saturates at low temperatures below 10 K [see inset of Fig. 9(c)].

The detailed temperature dependence of other Raman-active phonons is shown in Fig. S5 [25]. The classical anharmonic behavior, according to Eq. (3), is observed for most phonons, except the mode at 340 cm^{-1} which exhibits an anomalous temperature behavior, likely caused by a short-range magnetic order above T_{N1}.

IV. CONCLUSIONS

We observed the softening of a phonon in the THz range on cooling towards $T_2 = 460$ K, a temperature at which BiMn$_7$O$_{12}$ undergoes a structural phase transition from monoclinic $I2/m$ to a noncentrosymmetric monoclinic Im phase. At 300 K, this phonon also has an anomaly coinciding with another structural phase transition to the $P1$ phase, in which the polarization is predicted to move out of the ac plane. The observed behavior of the optical phonon is typical for

displacive ferroelectric phase transitions. Also, the microwave permittivity shows a peak at $T_3 = 290$ K, indicating the ferroelectric nature of the phase transition at this temperature. For experimental reasons, it was not possible to measure the microwave permittivity above 400 K, i.e., not near T_2 or T_1. Unfortunately, neither the polarization hysteresis loops nor the pyrocurrent could be measured due to the conductivity of the sample above 100 K, but the soft mode in THz and IR spectra clearly indicates signs of successive displacive ferroelectric phase transitions in the two polar phases Im and $P1$.

The results here presented are consistent with the recently reported temperature dependence of the polarization calculated from Mössbauer data for $BiMn_{6.96}Fe_{0.04}O_{12}$, showing a paraelectric to ferroelectric phase transition around 437 K, and a considerable increase in polarization below 270 K, with an extrapolated Curie temperature of 294 K [19].

The dielectric anomalies, measured at 5.8 GHz and in the 1–10 Hz range, observed near T_{N1} and T_{N3} are indicative of a strong magnetoelectric coupling at the magnetic phase transitions. This supports the conclusions of Ref. [18] that the polar magnetic phases are stabilized by trilinear magnetoelectric coupling via inverse exchange striction.

The Raman mode seen near $155\,cm^{-1}$ senses the structural phase transition at 300 K. Furthermore, some Raman modes sense the magnetic phase transitions occurring at 59, 55, and 27 K, showing that spin-phonon coupling is relevant in this compound in this temperature range. The highest-frequency mode observed near $660\,cm^{-1}$ exhibits a clear deviation from anharmonic temperature dependence, which is linearly correlated with the spin correlation function $\langle \boldsymbol{S_i} \cdot \boldsymbol{S_j} \rangle$.

ACKNOWLEDGMENTS

[1] A. N. Vasil'ev and O. S. Volkova, New functional materials $AC_3B_4O_{12}$ (Review), Low Temp. Phys. **33**, 895 (2007).

[2] I. Yamada, High-pressure synthesis, electronic states, and structure-property relationships of perovskite oxides, $ACu_3Fe_4O_{12}$ (A: Divalent alkaline earth or trivalent rare-earth ion), J. Ceram. Soc. Jpn. **122**, 846 (2014).

[3] A. A. Belik, Y. Matsushita, and D. D. Khalyavin, Reentrant structural transitions and collapse of charge and orbital orders in quadruple perovskites, Angew. Chem. **56**, 10423 (2017).

[4] J. Li, M. A. Subramanian, H. D. Rosenfeld, C. Y. Jones, B. H. Toby, and A. W. Sleight, Clues to the giant dielectric constant of $CaCu_3Ti_4O_{12}$ in the defect structure of "$SrCu_3Ti_4O_{12}$", Chem. Mater. **16**, 5223 (2004).

[5] C. C. Homes, T. Vogt, S. M. Shapiro, S. Wakimoto, and A. P. Ramirez, Optical response of high-dielectric-constant perovskite-related oxide, Science **293**, 673 (2001).

[6] R. D. Johnson, L. C. Chapon, D. D. Khalyavin, P. Manuel, P. G. Radaelli, and C. Martin, Giant improper ferroelectricity in the ferroaxial magnet $CaMn_7O_{12}$, Phys. Rev. Lett. **108**, 067201 (2012).

[7] A. Maia, C. Kadlec, M. Savinov, R. Vilarinho, J. A. Moreira, V. Bovtun, M. Kempa, M. Míšek, J. Kaštil, A. Prokhorov, J. Maňák, A. A. Belik, and S. Kamba, Can the ferroelectric soft mode trigger an antiferromagnetic phase transition? J. Eur. Ceram. Soc. **43**, 2479 (2023).

[8] I. Yamada, Novel catalytic properties of quadruple perovskites, Sci. Technol. Adv. Mater. **18**, 541 (2017).

[9] A. Prodi, E. Gilioli, A. Gauzzi, F. Licci, M. Marezio, F. Bolzoni, Q. Huang, A. Santoro, and J. W. Lynn, Charge, Orbital and spin ordering phenomena in the mixed valence manganite $NaMn_3^{3+})(Mn_2^{3+}Mn_2^{4+})O_{12}$, Nat. Mater. **3**, 48 (2004).

[10] A. Prodi, A. Daoud-Aladine, F. Gozzo, B. Schmitt, O. Lebedev, G. van Tendeloo, E. Gilioli, F. Bolzoni, H. Aruga-Katori, H. Takagi, M. Marezio, and A. Gauzzi, Commensurate structural modulation in the charge- and orbitally ordered phase of the quadruple perovskite $(NaMn_3)Mn_4O_{12}$, Phys. Rev. B **90**, 180101(R) (2014).

[11] M. Marezio, P. D. Dernier, J. Chenavas, and J. C. Joubert, High pressure synthesis and crystal structure of $NaMn_7O_{12}$, J. Solid State Chem. **6**, 16 (1973).

[12] B. Bochu, J. Chenavas, J. C. Joubert, and M. Marezio, High pressure synthesis and crystal structure of a new series of perovskite-like compounds CMn_7O_{12} (C = Na, Ca, Cd, Sr, La, Nd), J. Solid State Chem. **11**, 88 (1974).

[13] A. A. Belik, Y. Matsushita, Y. Kumagai, Y. Katsuya, M. Tanaka, S. Y. Stefanovich, B. I. Lazoryak, F. Oba, and K. Yamaura, Complex structural behavior of $BiMn_7O_{12}$ quadruple perovskite, Inorg. Chem. **56**, 12272 (2017).

[14] W. A. Sławiński, H. Okamoto, and H. Fjellvåg, Triclinic crystal structure distortion of multiferroic $BiMn_7O_{12}$, Acta Crystallogr. B: Struct. Sci. Cryst. Eng. Mater. **73**, 313 (2017).

[15] K. Momma and F. Izumi, VESTA 3 for three-dimensional visualization of crystal, volumetric and morphology data, J. Appl. Crystallogr. **44**, 1272 (2011).

[16] A. Gauzzi, G. Rousse, F. Mezzadri, G. L. Calestani, G. André, F. Bourée, M. Calicchio, E. Gilioli, R. Cabassi, F. Bolzoni, A. Prodi, P. Bordet, and M. Marezio, Magnetoelectric coupling driven by inverse magnetostriction in multiferroic $BiMn_3Mn_4O_{12}$, J. Appl. Phys. **113**, 043920 (2013).

[17] F. Mezzadri, M. Buzzi, C. Pernechele, G. Calestani, M. Solzi, A. Migliori, and E. Gilioli, Polymorphism and multiferroicity in $Bi_{1-x/3}(Mn_3^{III})(Mn_{4-x}^{III}Mn_x^{IV})O_{12}$, Chem. Mater. **23**, 3628 (2011).

[18] D. Behr, A. A. Belik, D. D. Khalyavin, and R. D. Johnson, $BiMn_7O_{12}$: Polar antiferromagnetism by inverse exchange striction, Phys. Rev. B **107**, L140402 (2023).

[19] V. I. Nitsenko, A. V. Sobolev, A. A. Belik, Y. S. Glazkova, and I. A. Presnyakov, Electric polarization in the $BiMn_7O_{12}$ quadruple manganite: A ^{57}Fe probe Mössbauer investigation, J. Exp. Theor. Phys. **136**, 620 (2023).

[20] A. V. Sobolev, V. I. Nitsenko, A. A. Belik, I. S. Glazkova, M. S. Kondratyeva, and I. A. Presniakov, Jahn–Teller ordering dynamics in the paraelectric $BiMn_7O_{12}$ phase: ^{57}Fe probe Mössbauer diagnostics, J. Exp. Theor. Phys. **137**, 404 (2023).

[21] D. D. Khalyavin, R. D. Johnson, F. Orlandi, P. G. Radaelli, P. Manuel, and A. A. Belik, Emergent helical texture of electric dipoles, Science **369**, 680 (2020).

[22] N. Imamura, M. Karppinen, T. Motohashi, D. Fu, M. Itoh, and H. Yamauchi, Positive and negative magnetodielectric effects in A-site ordered $(BiMn_3)Mn_4O_{12}$ perovskite, J. Am. Chem. Soc. **130**, 14948 (2008).

[23] N. Imamura, K. Singh, D. Pelloquin, C. Simon, T. Sasagawa, M. Karppinen, H. Yamauchi, and A. Maignan, Magnetodielectric response of square-coordinated MnO_2 unit in cubic $BiMn_7O_{12}$, Appl. Phys. Lett. **98**, 072903 (2011).

[24] F. Izumi and T. Ikeda, *A Rietveld-analysis Program RIETAN-98 and its Applications to Zeolites*, Materials Science Forum Vol. 321-324 (Trans Tech, Ltd, 2000), p. 198.

[25] See Supplemental Material at http://link.aps.org/supplemental/10.1103/PhysRevB.109.134111 for additional data on SEM images, magnetization, permittivity, and MIR spectrum. It also contains Refs. [22,23,26].

[26] F. Mezzadri, G. Calestani, M. Calicchio, E. Gilioli, F. Bolzoni, R. Cabassi, M. Marezio, and A. Migliori, Synthesis and characterization of multiferroic $BiMn_7O_{12}$, Phys. Rev. B **79**, 100106(R) (2009).

[27] V. Bovtun, V. Pashkov, M. Kempa, S. Kamba, A. Eremenko, V. Molchanov, Y. Poplavko, Y. Yakymenko, J. H. Lee, and D. G. Schlom, An electrode-free method of characterizing the microwave dielectric properties of high-permittivity thin films, J. Appl. Phys. **109**, 024106 (2011).

[28] V. Bovtun, S. Veljko, A. Axelsson, S. Kamba, N. Alford, and J. Petzelt, Microwave characterization of thin ferroelectric films without electrodes by composite dielectric resonator, Integr. Ferroelectr. **98**, 53 (2008).

[29] V. Skoromets, C. Kadlec, H. Němec, D. Fattakhova-Rohlfing, and P. Kužel, Tunable dielectric properties of $KTaO_3$ single crystals in the terahertz range, J. Phys. D: Appl. Phys. **49**, 065306 (2016).

[30] W. Hayes and R. Loudon, *Scattering of Light by Crystals* (Wiley-Interscience, New York, 1978), Vol. 47.

[31] M. Balkanski, R. F. Wallis, and E. Haro, Anharmonic effects in light scattering due to optical phonons in silicon, Phys. Rev. B **28**, 1928 (1983).

[32] A. B. Sushkov, O. Tchernyshyov, W. Ratcliff II, S. W. Cheong, and H. D. Drew, Probing spin correlations with phonons in the strongly frustrated magnet $ZnCr_2O_4$, Phys. Rev. Lett. **94**, 137202 (2005).

[33] M. I. Aroyo, J. M. Perez-Mato, D. Orobengoa, E. Tasci, G. De La Flor, and A. Kirov, Crystallography online: Bilbao crystallographic server, Bulg. Chem. Commun. **43**, 183 (2011).

[34] M. I. Aroyo, J. M. Perez-Mato, C. Capillas, E. Kroumova, S. Ivantchev, G. Madariaga, A. Kirov, and H. Wondratschek, Bilbao crystallographic server: I. Databases and crystallographic computing programs, Z. Kristallogr. Cryst. Mater. **221**, 15 (2006).

[35] M. I. Aroyo, A. Kirov, C. Capillas, J. M. Perez-Mato, and H. Wondratschek, Bilbao crystallographic server. II. Representations of crystallographic point groups and space groups, Acta Crystallogr., Sect. A **62**, 115 (2006).

[36] R. Vilarinho, E. C. Queirós, A. Almeida, P. B. Tavares, M. Guennou, J. Kreisel, and J. A. Moreira, Scaling spin–phonon and spin–spin interactions in magnetoelectric $Gd_{1-x}Y_xMnO_3$, J. Solid State Chem. **228**, 76 (2015).

[37] V. S. Bhadram, B. Joseph, D. Delmonte, E. Gilioli, B. Baptiste, Y. Le Godec, R. P. S. M. Lobo, and A. Gauzzi, Pressure-induced structural phase transition and suppression of Jahn-Teller distortion in the quadruple perovskite structure, Phys. Rev. Mater. **5**, 104411 (2021).